Environmental Advances 16 (2024) 100525

Contents lists available at ScienceDirect

Environmental Advances

journal homepage: www.sciencedirect.com/journal/environmental-advances

Transport and deposition of microplastics and nanoplastics in the human respiratory tract

Xinlei Huang [a], Suvash C. Saha [a,*], Goutam Saha [a,b], Isabella Francis [a], Zhen Luo [a]

[a] School of Mechanical and Mechatronic Engineering, University of Technology Sydney, New South Wales 2007, Australia
[b] Department of Mathematics, University of Dhaka, Dhaka 1000, Bangladesh

ARTICLE INFO

Keywords:
Microplastics
Nanoplastics
Respiratory tract
Computational fluid particle dynamics
Biofluid
Particle laden fluid

ABSTRACT

Recent studies have unveiled the presence of nano- and microplastics (NMPs) within both human and avian respiratory systems, prompting an exploration into the interactions between these particles and the human respiratory system. Experimental evidence has strongly suggested that these plastic particles amplify human susceptibility to a spectrum of lung disorders, including chronic obstructive pulmonary disease, fibrosis, dyspnea, asthma, and the formation of frosted glass nodules. To advance the understanding, this study employs computational fluid-particle dynamics (CFPD) to study the transfer and deposition of poly-dispersed 1-100 nm nanoplastics and 1-100 μm microplastics under three breathing conditions. Notably, this investigation utilized a computerized tomography-based full respiratory tract model, comprehensively spanning regions from the nasal cavity to the 13th generation of the bronchial tree, providing a highly detailed representation of the anatomical complexities of the human respiratory system. The outcomes reveal distinctive deposition patterns of spherical, cylindrical, and tetrahedral NMPs in the human respiratory tract, elucidating the significant impact of breathing rate, pinpointing specific deposition hotspots, and highlighting the critical role of particle size in governing transport and deposition behavior. This study establishes a link between the behavior of nanoplastics within the respiratory tract and its consequential impact, providing insights that extend across three critical domains. Firstly, in environmental health, the research contributes to understanding NMP-related air pollution. Secondly, within respiratory medicine, the findings shed light on NMPs' role in respiratory disorders. Finally, this study guides the formulation of regulations addressing permissible NMP levels and mitigating associated health and environmental risks.

Introduction

Microplastics (MPs) are characterized by their diminutive particle size, typically measuring less than 5 mm in diameter (Prata et al., 2020; Feng et al., 2023). Nanoplastics (NPs) are defined by their even more minuscule dimensions, conventionally regarded as having a particle size falling within the range of 1 and 100 nm. Nano- and microplastics (NMPs) can be categorized based on the origin of their source into two classes (Liu et al., 2019). The primary NMPs are intentionally manufactured, including a wide array of cosmetics (Saha and Saha, 2024) and personal care products such as toothpaste (Napper et al., 2015). The secondary NMPs comprise fragments derived from the degradation of larger plastic products, encompassing items such as water bottles (Yang and Wang, 2023), food containers (Du et al., 2020), and clothes (Browne et al., 2011).

Respiratory exposure to small particles has consistently been recognized as a significant public health concern. Extensive research indicates that lung injuries resulting from the inhalation of smoke or chemical combustion products are closely associated with considerable morbidity and mortality (Dries and Endorf, 2013). Furthermore, numerous studies have documented the relationship between exposure to small dust particles and mortality (Hashizume et al., 2020). Respiratory inhalation ranks as the second most likely pathway for human exposure to NPs (Yee et al., 2021). Extensive investigations have identified synthetic textiles as a principal source of indoor airborne plastic particles (Stapleton, 2019), while the outdoor environment presents a multitude of sources encompassing contaminated aerosols from the ocean to particles originating from wastewater treatment (Lehner et al., 2019; Zhang et al., 2021). Recent experiments have uncovered the presence of MPs within the human respiratory tract, spanning from the nasal cavity (Jiang et al., 2022) to the lower airway (Baeza-Martinez

* Corresponding author.
E-mail address: Suvash.Saha@uts.edu.au (S.C. Saha).

https://doi.org/10.1016/j.envadv.2024.100525
Received 6 March 2024; Accepted 26 March 2024
Available online 27 March 2024

Nomenclature

A_p	projected particle surface area
C_{RL}	rotational lift coefficient
d_{ij}	deformation tensor
d_p	particle diameter (m)
E	energy (J)
g	gravitational acceleration, in the negative z-direction (ms^{-2})
G_b	turbulence generation due to buoyancy
$G_{\omega b}$	turbulence generation due to buoyancy for ω equation
h_j	enthalpy of species j (J)
J_j	diffusion flux of species j
K	model constant, K=2.594
k	turbulent kinetic energy (m^2s^{-2})
k_{eff}	effective conductivity (m^2s^{-2})
p	static pressure (Pa)
P_k	rate of production of turbulent kinetic energy
P_ω	rate of production of specific dissipation rate
Re_r	relative Reynolds number
S_0	spectral intensity
S_{ij}	mean component of the rate of deformation s_{ij}
T	the absolute temperature of the fluid (K)
t	time (s)
u	fluid velocity (ms^{-1})
u_p	particle velocity (ms^{-1})
V	relative fluid - particle velocity (ms^{-1})
Y_k	dissipation of turbulent kinetic energy due to turbulence
Y_ω	dissipation of specific dissipation rate due to turbulence

Greek symbols

σ_k	turbulent Prandtl numbers for turbulent kinetic energy
σ_ω	turbulent Prandtl numbers for specific dissipation rate
δ_{ij}	Kronecker delta ($\delta_{ij} = 1$, if $i = j$; $\delta_{ij} = 0$, if $i \neq j$)
ζ	zero-mean, unit-variance Gaussian random number
λ	molecular mean free path (65 nm)
μ	molecular viscosity of the fluid (Nsm^{-2})
μ_t	turbulent viscosity (Nsm^{-2})
ν	kinematic viscosity of the fluid (m^2s^{-1})
ρ	fluid density (kgm^{-3})
$\bar{\bar{\tau}}$	stress tensor (Pa)
$\bar{\bar{\tau}}_{eff}$	effective stress tensor (Pa)
ω	specific dissipation rate (s^{-1})
Ω	relative fluid-particle angular velocity ($rads^{-1}$)

et al., 2022; Jenner et al., 2022; Lu et al., 2023). Notably, the ubiquity of MPs extends beyond humans, as they have been discerned in diverse animal species, including wild avian populations in Japan (Tokunaga et al., 2023).

The pervasive occurrence of airborne plastics in the environment has given rise to legitimate concerns regarding their potential effect on human respiratory health, as the World Health Organization calls for more research into MPs (Osseiran, 2019). Recent investigations into the interplay between NMPs and human lung cells have provided compelling evidence suggesting that NMPs may exert a notable influence on endogenous surfactants and cytoskeleton rearrangement, thereby amplifying human susceptibility to a spectrum of debilitating lung disorders, encompassing chronic obstructive pulmonary disease, fibrosis, dyspnea, asthma, and the formation of frosted glass nodules (Chen et al., 2022; Zuo et al., 2008; Li et al., 2022; Dong et al., 2020; Shi et al., 2022).

The application of computational fluid-particle dynamics (CFPD) stands as a promising method for the numerical investigation of NMPs. In contrast to in vivo experiments, the in-silico approach has demonstrated remarkable efficiency in forecasting the trajectories of inhaled particles, all the while eliminating potential risks to human subjects. Moreover, it serves as a valuable tool for healthcare professionals, enabling them to discern the consequences of particle deposition within the human respiratory system. Previous research endeavors have employed CFPD to successfully predict the intricate dynamics governing the transport and deposition (TD) of nano- and micropollutants, as well as pharmaceutical aerosols, within specific segments of the human respiratory tract (Ahookhosh et al., 2019; Islam et al., 2017; Khajeh-Hosseini-Dalasm and Longest, 2015; Koullapis et al., 2020; Longest et al., 2019; Ma and Lutchen, 2009; Worth Longest and Vinchurkar, 2007; Xi and Longest, 2009). Recent CFPD studies have witnessed a significant increase in investigations concerning NMPs within various environments, including open channel flows (Sakai and Manhart, 2024), turbulent flows (Shamskhany and Karimpour, 2022), streams (Yang and Foroutan, 2023), quiescent waters (Zhang et al., 2023), coastal waters (Fatahi et al., 2021), lakes (Elagami et al., 2023), the hyporheic zone (Dichgans et al., 2023), wave tanks (Quyen and Choi, 2022), and over the slopes (Quyen et al., 2024). However, there appears to be a notable deficiency in CFPD research focusing on NMPs within the context of the respiratory system.

In a recent study by Islam et al. (2023), pioneering efforts were made in conducting numerical predictions of the TD of MPs in a human upper airway model spanning from the nasal cavity to the upper trachea under two steady-state airflow conditions. While the study represents a significant advancement in our understanding of MP behavior within the respiratory system, there are notable gaps that should be addressed: Firstly, the investigation primarily focused on the human upper airway. Nevertheless, the incorporation of a full respiratory tract model would offer a holistic perspective on the TD patterns of plastic particles throughout the entirety of the respiratory tract, providing a more complete portrayal of the dynamics involved. Secondly, the study limited its consideration to mono-dispersed MPs with three specific diameters (1.6, 2.56, and 5.56 μm). A more comprehensive analysis could encompass a wider range of particle sizes, mirroring the diversity of MP dimensions encountered in real-world scenarios. Lastly, the utilization of a transient respiration breathing airflow, rather than a steady-state airflow condition, holds the potential to yield more realistic simulation results.

The objective of the current investigation is to provide predictive insights into the TD behavior of spherical, cylindrical, and tetrahedral NMPs within a full respiratory tract model under three realistic transient respiration breathing patterns. To capture the diverse spectrum of particle sizes encountered in practical scenarios, a poly-disperse methodology is employed, simultaneously releasing particles spanning a range of 100 different diameters. Specifically, the particle size distribution extends from 1 to 100 nm for NPs, and from 1 to 100 μm for MPs. Central to this study is the utilization of a state-of-the-art CT-based full respiratory tract model, encompassing the entirety of the respiratory system from the nasal cavity down to the 13th generation of the bronchial tree. This comprehensive model facilitates a comprehensive examination of the TD patterns exhibited by NMPs throughout the entire respiratory tract. Furthermore, to enhance the realism of airflow dynamics predictions, experimentally measured respiration volume flow rates are incorporated. Specifically, this study examines three breathing scenarios: slow, middle, and fast, which correspond to resting, normal, and running conditions, respectively. By implementing the above improvements, the simulations faithfully replicate those observed in real-life

respiration, thus reinforcing the validity and authenticity of the findings.

Methodology

Computational model and discretization scheme

This study involves the creation of a computational model for the respiratory pathway, as outlined in our previous work (Saha et al., 2022). The finalized respiratory system model is depicted in Fig. 1. To facilitate the process of meshing and modeling, we simplified the respiratory tract anatomy to encompass critical components, including the nasal cavity, nasopharynx, oral cavity, oropharynx, laryngopharynx, larynx, and airways from generation 0 to generation 13.

The current study employs an advanced polyhedral hybrid meshing technique, as depicted in Fig. 1(a) and (b). The mesh predominantly consists of irregular polyhedral cells arranged in four layers of polyhedral prisms, resulting in a total cell count of 7.61 million. A non-uniform density mesh design is implemented to optimize computational efficiency. Denser node distributions are strategically placed in regions with elevated turbulent intensity (Kumar et al., 2019) and intricate geometric attributes. Notably, the mean nodal spacing varies, measuring 0.4 mm for the upper airway, 0.35 mm for G0 and G1, and 0.2 mm for the smaller branches spanning G3–G13 of the bronchial tree. The initial boundary layer cell height is set at 0.1 times the local nodal distance, leading to a dynamically varying boundary layer cell thickness across the model, as illustrated in Fig. 1(a) and (b).

Governing equations

This study tackles airflow turbulence within the continuum phase by employing the k-ω Shear-Stress Transport (SST) model to solve the Reynolds-averaged Navier–Stokes equations. Simultaneously, the discrete phase model is utilized for simulating both nano- and microplastics. Significantly, the modeling approach encompasses the energy equation for the continuum phase and incorporates Brownian motion modeling to calculate the force balance of sub-micron particles precisely.

Governing equations of the continuum phase (ANSYS, 2020):

Continuity equation:

$$\frac{\partial \rho}{\partial t} + \nabla \cdot (\rho \boldsymbol{u}) = 0 \tag{1}$$

Momentum equation:

$$\frac{\partial \rho \boldsymbol{u}}{\partial t} + \nabla \cdot (\rho \boldsymbol{u}\boldsymbol{u}) = -\nabla p + \nabla \cdot \bar{\bar{\tau}} + \rho \boldsymbol{g} \tag{2}$$

The turbulence kinetic energy (k) equation:

$$\frac{\partial (\rho k)}{\partial t} + \frac{\partial (\rho k u_i)}{\partial x_i} = \frac{\partial}{\partial x_j}\left[\left(\mu + \frac{\mu_t}{\sigma_k}\right)\frac{\partial k}{\partial x_j}\right] + P_k - Y_k + G_b \tag{3}$$

The specific dissipation rate (ω) equation:

$$\frac{\partial (\rho \omega)}{\partial t} + \frac{\partial (\rho \omega u_i)}{\partial x_i} = \frac{\partial}{\partial x_j}\left[\left(\mu + \frac{\mu_t}{\sigma_\omega}\right)\frac{\partial \omega}{\partial x_j}\right] + P_\omega - Y_\omega + G_{\omega b} \tag{4}$$

Energy equation:

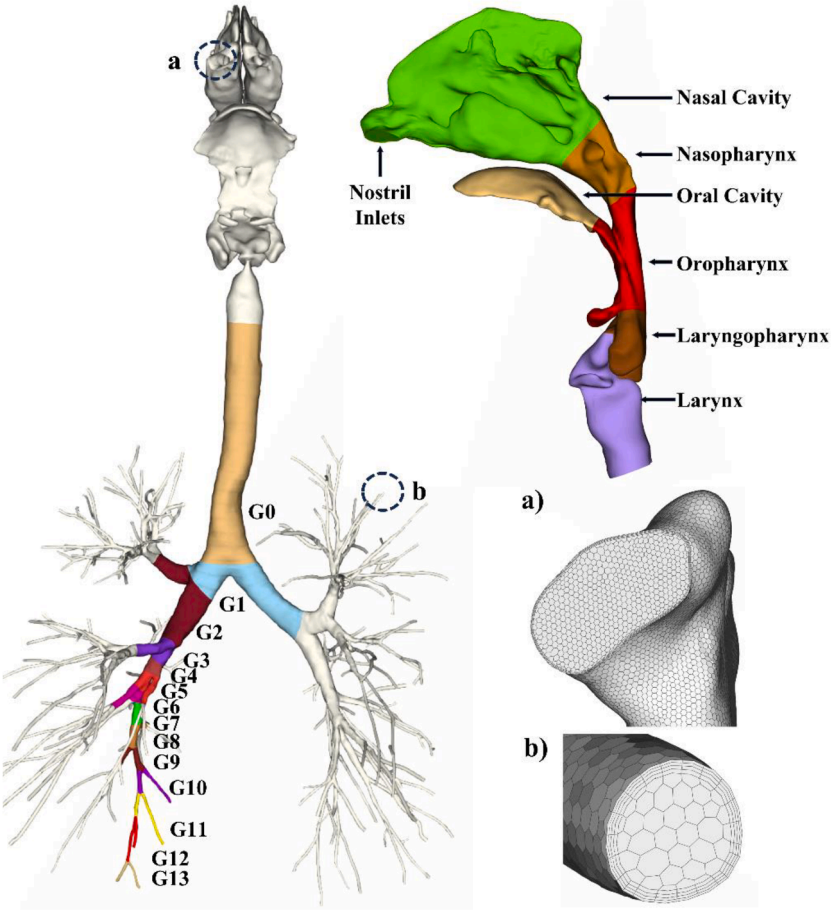

Fig. 1. Computational model of the respiratory tract, featuring detailed views of the mesh at the (a) Inlet of the right nostril and (b) One of the outlets in the left superior lobe.

$$\frac{\partial \rho E}{\partial t} + \nabla \cdot (\boldsymbol{u}(\rho E + p)) = \nabla \left(k_{eff} \nabla T - \sum_j h_j \boldsymbol{J}_j + \left(\bar{\bar{\tau}}_{eff} \cdot \boldsymbol{u} \right) \right) \quad (5)$$

Governing equations of the discrete phase (ANSYS, 2020):
Particle force balance equation:

$$m_p \frac{\partial u_p}{\partial t} = F_{drag} + F_{gravitation} + F_{Brownian} + F_{Saffman} + F_{Magnus} \quad (6)$$

The drag force is:

$$F_{drag} = m_p \frac{u - u_p}{\tau_r} \quad (7)$$

The gravitational force is:

$$F_{gravitation} = m_p g \frac{\rho_p - \rho}{\rho_p} \quad (8)$$

The Brownian force acting on sub-micron particles is:

$$F_{Brownian} = m_p \zeta \sqrt{\frac{\pi S_0}{\Delta t}} \quad (9)$$

The Saffman's lift force acting on sub- micron particles is:

$$F_{Saffman} = m_p \frac{2K\nu^{1/2}\rho d_{ij}}{\rho_p d_p (d_{lk} d_{kl})^{1/4}} (u - u_p) \quad (10)$$

The Magnus lift force is:

$$F_{Magnus} = \frac{1}{2} A_p C_{RL} \rho_f \frac{|V|}{|\Omega|} (V \times \Omega) \quad (11)$$

Numerical modeling specifics

Comprehensive details concerning boundary conditions, material properties, and particle configurations are available in Table 1. The experimentally measured volume flow rate (Fig. 2) is multiplied by the nostril inlet area to formulate a realistic inlet velocity profile. Simulation durations vary: 1 second for a rapid breathing pattern at 60 breaths per minute (BPM), 2 seconds for a median breathing pattern at 30 BPM, and 4 seconds for a slow breathing pattern at 15 BPM, as depicted in Fig. 2. A study by Kolanjiyil and Kleinstreuer (2017) indicates that a 50,000 particle per second release rate is sufficient to achieve particle independence. Therefore, this study releases 80,000 particles at a rate of 4×10^5 particles per second during inhalation.

Mesh independence test

To assess mesh independence, incremental refinements are implemented by augmenting the mesh resolution by a factor of 1.5 in two successive steps. Table 2 outlines the convergence pattern observed in the area-averaged static pressure of the nasal cavity and the mass flow rate exiting the left inferior bronchi. The results indicate minimal variations in the considered variable across all meshes, with residuals consistently below 1% for every case. This empirical evidence substantiates that the mesh, comprised of 7.61 million cells in this study, ensures a state of mesh independence.

Experimental Validation

The computation of the total flow percentage is performed and compared with both prior experimental and CFD data, as detailed in Table 3. This comparison shows that the current simulation outcomes consistently lie within, or in close vicinity to, the range of previous experimental and CFD data. This alignment reinforce the credibility of the current simulation.

Table 1
Boundary conditions and material properties of the simulation.

Names	Value (Unit)	Refs.
Inlet Velocity	Realistic velocity profile	Nishi (2004)
Outlet Pressure	0 (Pa)	Saha et al. (2022)
Simulation Time	1, 2, 4 (s)	Nishi (2004)
Air density	1.225	-
Air dynamic viscosity	1.7894×10^{-5}	-
Particle density	940	Islam et al. (2023)
DPM tracking scheme	Implicit Euler (low order) and semi-implicit trapezoidal (high order)	ANSYS (2020)
Forces on particles	Drag (Eq. (7)), gravity (Eq. (8)), Brownian (Eq. (9)), Saffman's lift (Eq. (10)), Magnus lift (Eq. (11))	ANSYS (2020)
Cunningham correction	Included	ANSYS (2020)
Wall interaction	Trap	-
Turbulent dispersion	Discrete random walk	ANSYS (2020)
Number of particles	80,000	Kolanjiyil and Kleinstreuer (2017)
Particle release rate	4×10^5 (Napper et al., 2015) particles per second	Kolanjiyil and Kleinstreuer (2017)
Particle diameter (μm)	1–100 μm and 1–100 nm	-
Number of diameters	100	-
Number of particles per diameter	800	-
Particle diameter distribution	Rosin-Rammler (spread: 3.5)	ANSYS (2020)
Drag law for microparticles	Spherical & Non- Spherical	ANSYS (2020)
Shape factor of cylindrical particles	0.874	Islam et al. (2023)
Shape factor of tetrahedral particles	0.671	Islam et al. (2023)
Drag law for nanoparticles	Stokes-Cunningham	ANSYS (2020)
Rotational drag law	Dennis et al.	ANSYS (2020)
Magnus lift law	Oesterle-Bui-Dinh	ANSYS (2020)
Release type	Surface release, normal direction	-
Release start time	0 (s)	-
Release end time	0.2 (s)	-
Particle time step size	0.001 (s)	-

Results and discussion

Deposition patterns of spherical nanoplastics and microplastics

The deposition patterns of NMPs are vividly illustrated through scatter-histogram charts, wherein each NMP is represented as a uniquely colored sphere corresponding to its assigned group based on diameter. These spheres are positioned at precise deposition sites within the respiratory tract, highlighting their interactions with the mucus layer. Furthermore, the histograms and deposition charts accompanying each figure underscore the size-dependent and shape-dependent deposition rates. The varied distribution patterns observed in these histograms highlight the significant impact of particle diameter and respiration rate on deposition efficiency and location. Fig. 3 delves into the deposition patterns of NMPs under fast (running) breathing conditions. In Fig. 3(a), a concentration of larger MPs is observed in the anterior segment of the nasal cavity, indicated by a cluster of red-colored particles. Specifically, MPs with 41–100 μm diameters accumulate above the nostril inlet. Conversely, the larynx region shows a prevalence of blue-colored spheres, signifying smaller MP deposition, particularly within the 1–10 μm range. This observation aligns with fluid dynamics principles, where inertial impaction and gravitational settling predominantly influence larger MPs' deposition, particularly in high-velocity airstreams

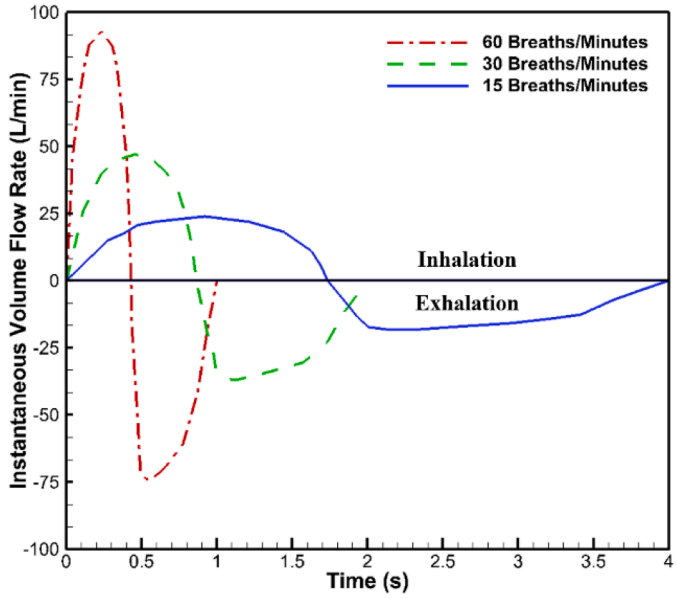

Fig. 2. Volume flow rate profiles for realistic breathing patterns at different rates (60 BPM for rapid, 30 BPM for median, and 15 BPM for slow), as experimentally determined by Nishi (2004) and implemented in CFD by Wedel et al. (2022).

Table 2
Mesh independence evaluation of the area-averaged static pressure of the nasal cavity and the mass flow rate exiting the left inferior bronchi at 0.01 s.

	Mesh Cells (in millions)	Static Pressure (*Pa*)	Mass Flow Rate (*g/s*)
Mesh 1	3.94	109.67	-0.067413939
Mesh 2	5.36	109.25	-0.067416437
Residual		0.38%	0.0037%
Mesh 2	5.36	109.25	-0.067416437
Mesh 3	7.61	108.38	-0.067063423
Residual		0.8%	0.525%

Table 3
Comparison of the total flow percentage with previous experimental measurements and numerical simulation.

Total Flow (%)	Previous Experiments		Previous CFD	Present CFD	
Regions	Cohen et al. (1990)	Horsfield et al. (1971)	Islam et al. (2017)	Slow at 1.23s*	Median at 0.321s
Left superior lobe	15.9	20.5	23.38	21.67	21.16
Left inferior lobe	23.9	24.9	21.82	25.80	25.03
Right superior lobe	18.2	21.7	21.03	17.78	17.93
Right middle lobe	9.6	9.6	9.953	10.92	11.21
Right inferior lobe	32.4	23.2	23.95	23.83	24.67
Left lung	39.8	45.4	45.20	47.47	46.19
Right lung	60.2	54.6	54.93	52.53	53.81

*Values calculated at the time step.

during rapid breathing. Fig. 3(b) reveals distinct differences in the deposition patterns of NPs compared to MPs. NPs display a more uniform distribution along airway walls, contrasting with the limited coverage observed for MPs in the posterior nasal cavity. NPs of various diameters exhibit a high degree of similarity in distribution patterns, indicating a more even dispersion compared to MPs. The larynx region exhibits as a prominent deposition site for NPs, reflecting the significant influence of Brownian motion on smaller particles and their more uniform distribution across slower and more turbulent airflow regions.

Fig. 3(c) shifts the focus to MPs in the lower airway. Notably, larger particles settle in the upper airways, with a fraction reaching the lower airway. MPs in the 1–6 μm range exhibit an even distribution from the 3rd to the 13th generation of bronchi, a phenomenon attributed to the combined effects of sedimentation and diffusion. The interplay of these forces results in the observed consistent deposition of smaller MPs throughout the lower respiratory tract. Examining Fig. 3(d), a parallel to Fig. 3(b) is evident, with NPs displaying an even higher degree of uniformity in their distribution patterns. Closer inspection reveals the clustering of NPs within the trachea and primary bronchi, emphasizing the combined effect of turbulent eddies and diffusional transport. Moreover, lobe-specific variations in NP distribution suggest the complex interaction between respiratory anatomy, airflow dynamics, and particle physics. The observed variability between lobes underlines the importance of considering anatomical asymmetry and individual differences in the computational modeling of particle deposition.

The deposition patterns of NMPs under normal (middle) breathing conditions are delineated in Fig. 4. In Fig. 4(a), the deposition pattern for more prominent MPs with diameters ranging from 41 to 100 μm is notably different from that observed during fast breathing. Instead of a concentrated area above the nostril inlet, there's a more extensive deposition region spanning 4 by 4 centimeters. This expanded area is attributed to the decreased velocity and turbulence of inhaled air during normal breathing, facilitating a gentler and more widespread distribution of particles. An interesting observation is the presence of 91–100 μm MPs within the posterior nasal cavity, a phenomenon absent during fast breathing. Additionally, there's an upsurge in the deposition of smaller MPs (1–40 μm diameter) in the upper airway, particularly in the lower nasal cavity and posterior nasopharynx and oropharynx regions, where minimal deposition occurred during fast respiration. The increased deposition of smaller particles in these regions is attributed to altered airflow patterns and reduced inertial impaction at slower breathing rates, allowing particles more time to settle and diffuse under the influence of gravity. In Fig. 4(b), the deposition pattern of NPs in the upper airway during normal breathing conditions displays reduced coverage compared to fast breathing. A distinct concentration point at the oropharynx becomes pronounced, a phenomenon not observed in the deposition pattern of MPs. The reduced range and focused deposition of NPs in specific areas under normal breathing conditions are linked to altered airflow dynamics, where slower velocities and less turbulent flow patterns favor more localized deposition influenced by Brownian motion and the airway's anatomical structure.

Moving to Fig. 4(c), a notable observation is the prominence of larger MPs (9 and 10 μm red spheres) within the tracheobronchial tree. This contrasts with the absence of 10 μm MPs in the lower airway deposition pattern during fast breathing, indicating that the normal breathing pattern facilitates the downstream transport of MPs into deeper lung generations. Examining Fig. 4(d), a consistent trend emerges in the deposition of NPs in the lower airway, resembling the pattern observed in the upper airway. The overall reduction in deposition numbers highlights the five clusters of NPs identified during fast breathing. This delicate balance between aerodynamic drag forces and gravitational settling, modulated by breathing rate, suggests that at middle breathing rates, airflow is slow enough to allow gravity to guide larger particles more effectively into the deeper lung regions yet fast enough to prevent the majority from settling in the upper airways, as seen in slow breathing conditions.

Fig. 5 unveils the deposition patterns of NMPs during conditions of slow, resting respiration. In Fig. 5(a), a striking difference in MP deposition within the upper airway under slow breathing conditions

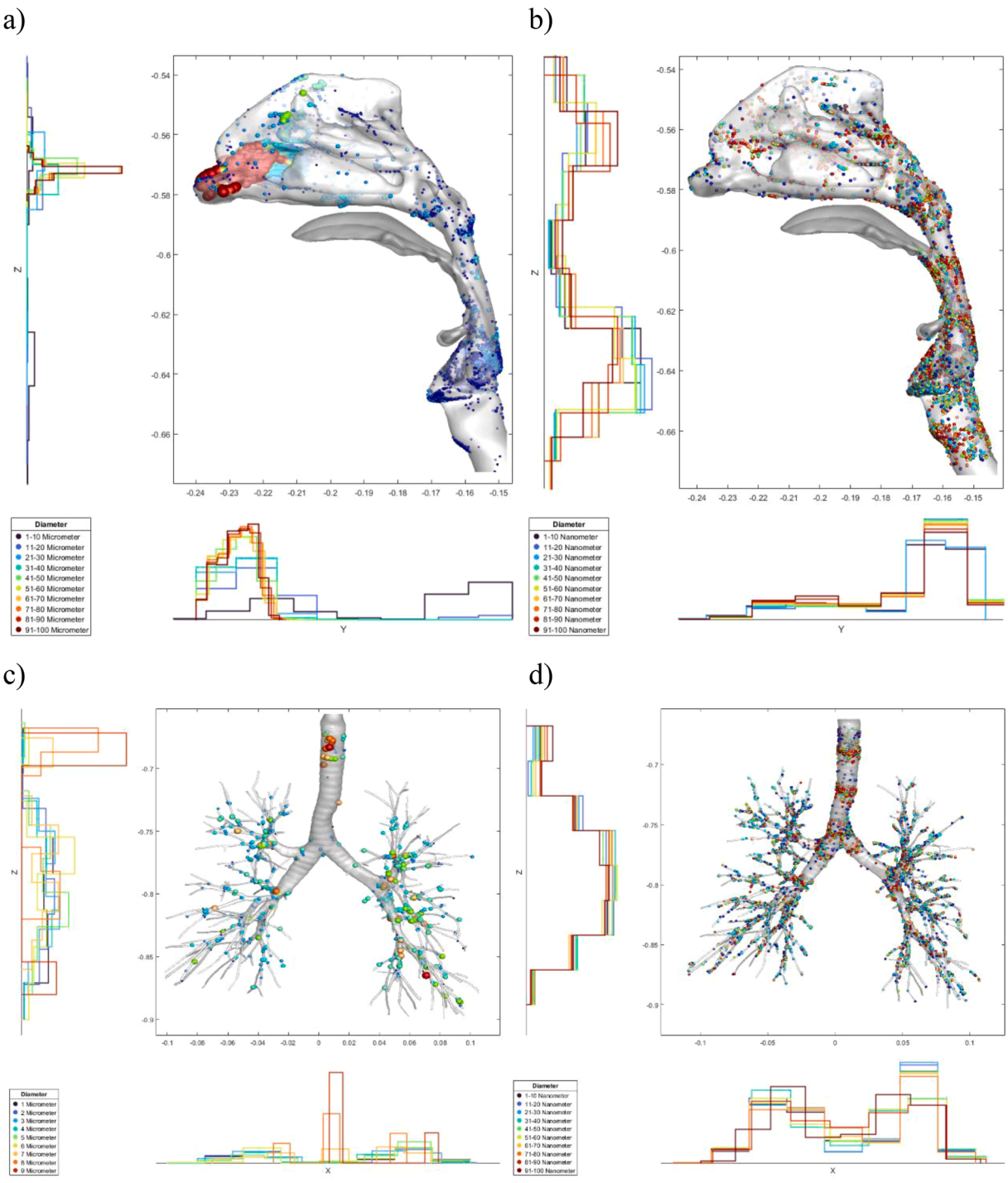

Fig. 3. Deposition pattern of NMPs at fast (running) breathing conditions. (a) Deposition of 1–100 μm MPs in the upper airways, (b) deposition of 1–100 nm NPs in the upper airways, (c) deposition of 1–10 μm MPs in the lower airways, and (d) deposition of 1–100 nm NPs in the lower airways.

compared to fast and moderate rates is immediately apparent. Notably, the nasal cavity exhibits extensive MP coverage, with approximately half of its surface area occupied by MPs. This broad coverage is attributed to significantly lower airflow rates during slow respiration, reducing inertial impaction and favoring gravitational settling, especially for larger MPs (61–100 μm). Larger MPs are predominantly located in the anterior section of the nasal cavity, while smaller MPs (1–40 μm) occupy the middle portion. Unlike faster breathing conditions, MPs with diameters between 41 and 60 μm exhibit a dispersed deposition pattern, notably in the middle and superior turbinate and the posterior region of the nasopharynx. This dispersion may result from the interplay between Brownian motion affecting smaller MPs and gravitational settling more pronounced for larger MPs, contributing to a varied distribution. In contrast, Fig. 5(b) reveals a substantial decrease in NP deposition under slow breathing conditions. Despite the overall reduction, the distribution of NPs stratified by diameter maintains consistent uniformity, highlighting the prominent role of Brownian motion in governing NP behavior with less influence from airflow patterns. Concentration sites for deposited NPs remain evident in the middle oropharynx and regions above and below the vocal cords, underscoring the impact of anatomical structures creating local eddies and flow patterns favoring NP deposition.

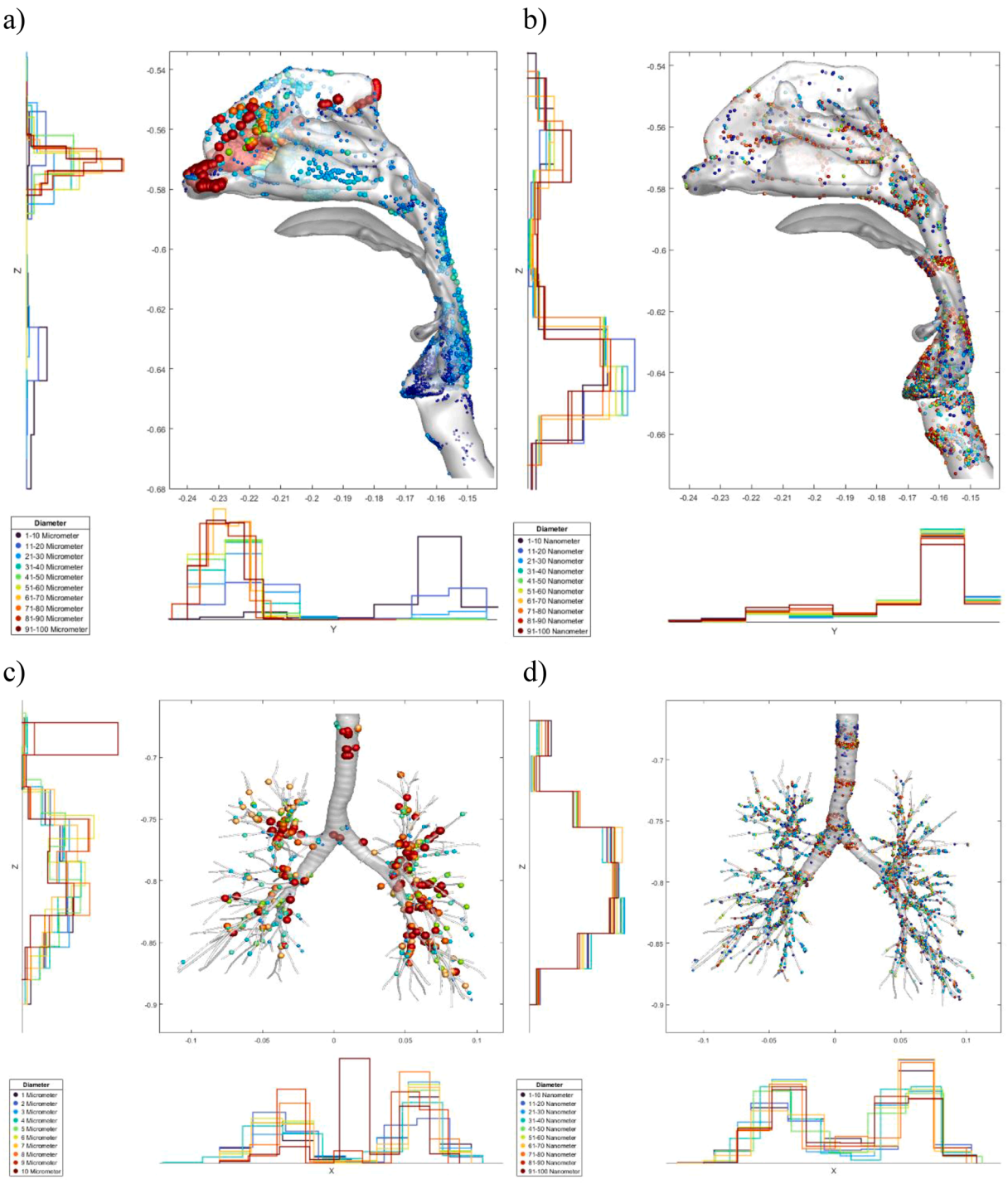

Fig. 4. Deposition pattern of NMPs at middle (normal) breathing condition. (a) Deposition of 1–100 μm MPs in the upper airways, (b) deposition of 1–100 nm NPs in the upper airways, (c) deposition of 1–9 μm MPs in the lower airways, and (d) deposition of 1–100 nm NPs in the lower airways.

Fig. 5(c) reveals significantly larger deposited MPs, represented by black spheres. A concentration of black spheres is observed at the upper trachea. MPs exceeding 9 μm show a propensity for deposition within the left lung lobes, while smaller counterparts accumulate within the right lung lobes. This selective deposition is explained by slight asymmetries in the respiratory tract, where varying flow dynamics and gravitational forces influence particle trajectories. The slower breathing rate enhances the effect of these asymmetries, resulting in observed lobe-specific deposition patterns. In Fig. 5(d), the NP deposition pattern parallels that of fast and moderate breathing conditions, yet a further reduction in the number of deposited NPs is evident under slow respiration. This reduction is likely due to decreased overall airflow, limiting NP transport deeper into the respiratory tract and promoting concentrated deposition in specific areas. The slow air movement allows more time for NPs to diffuse and settle, contributing to a more focused deposition pattern.

Deposition and escape fraction of nanoplastics and microplastics

The deposition fraction (DF) is defined as follows:

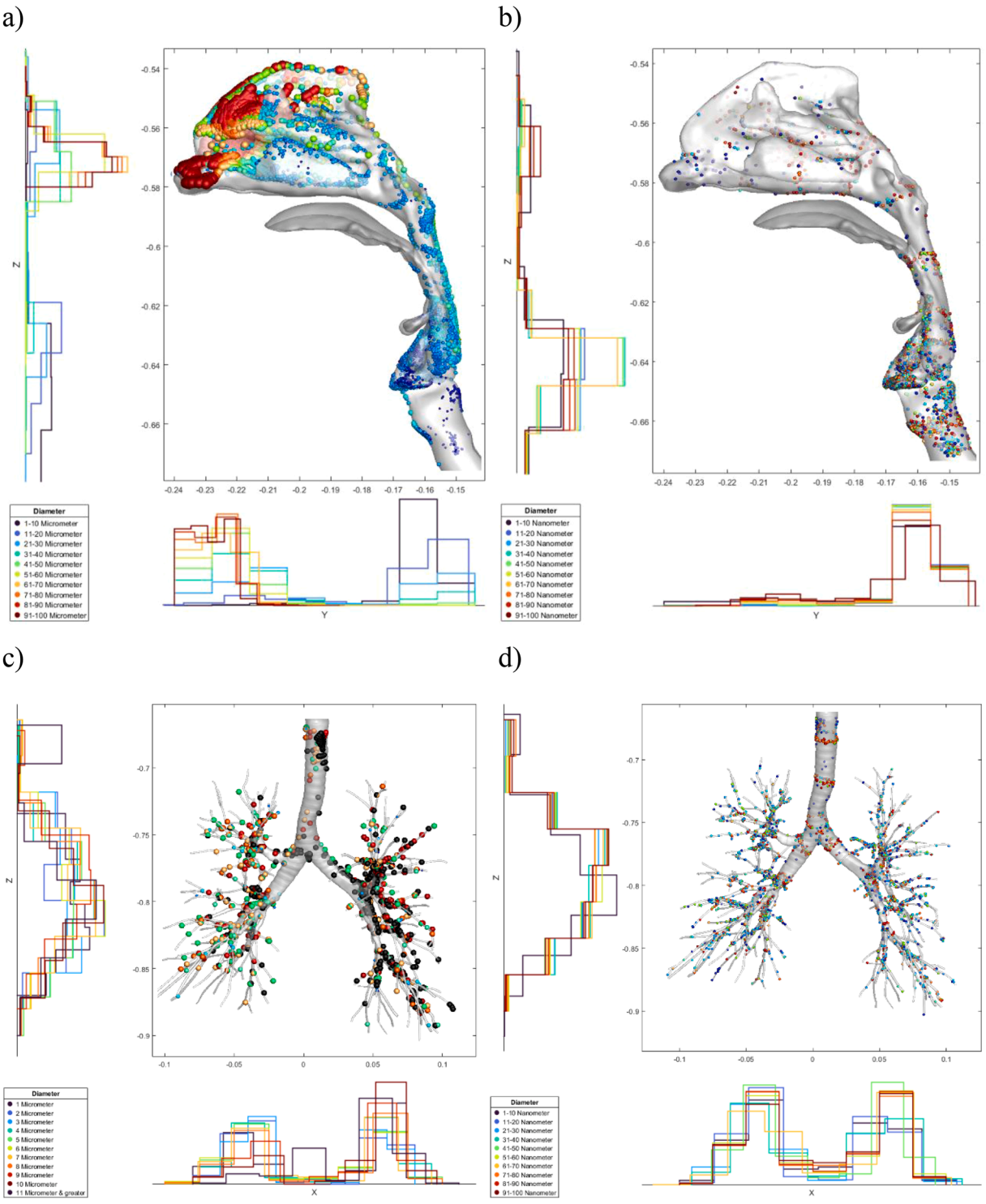

Fig. 5. Deposition pattern of NMPs at slow (resting) breathing conditions. (a) Deposition of 1–100 μm MPs in the upper asirways, (b) deposition of 1–100 nm NPs in the upper airways, (c) deposition of 1–11 μm and greater MPs in the lower airways, and (d) deposition of 1–100 nm NPs in the lower airways.

$$DF = \frac{Mass\ of\ deposited\ particle\ with\ targeted\ diameter}{Total\ mass\ of\ particle\ with\ targeted\ diameter\ released} \tag{12}$$

The escape fraction (EF) is defined as follows:

$$EF = \frac{Mass\ of\ escaped\ particle\ with\ targeted\ diameter}{Total\ mass\ of\ particle\ with\ targeted\ diameter\ released} \tag{13}$$

Fig. 6 depicts the deposition and escape fractions of NPs under various breathing conditions. In Fig. 6(a), rapid breathing exposes distinct deposition and escape hotspots. Larger NPs (81–100 nm) significantly deposit in the nasal cavity (14.2–17.8%), influenced by inertial impaction, while smaller NPs (11–30 nm) escape more in the left inferior region (about 13%), driven by Brownian diffusion. The laryngopharynx and larynx consistently maintain higher deposition (exceeding 8%) in the upper airway, while lower airways G6 and G7 exhibit the highest deposition (4–6.7%) across NP sizes. Right middle lobe outlets consistently show the lowest escape (below 3.4%), and smaller NPs (1–10 nm) exhibit lower escape than those in the 11–20 nm

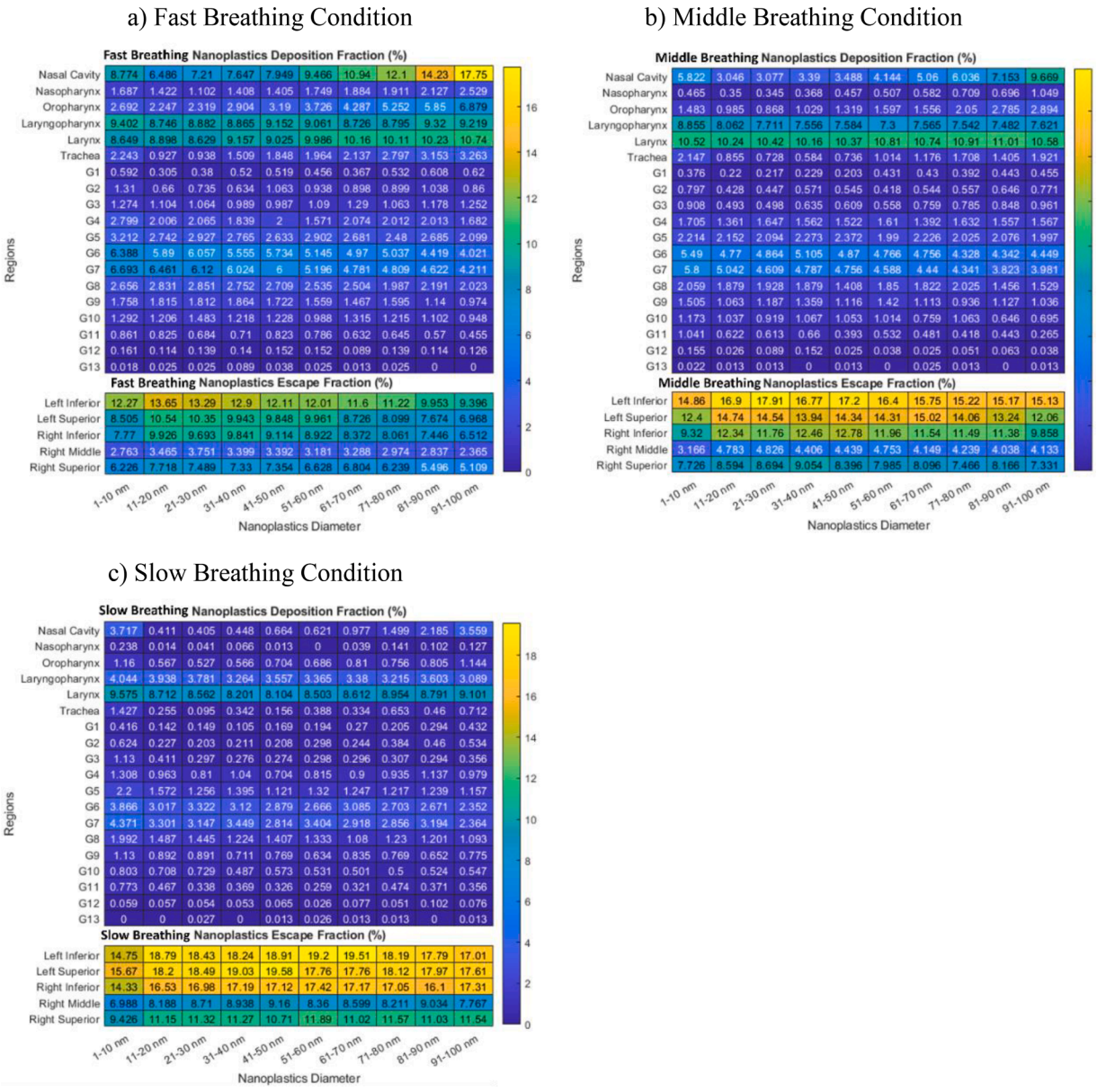

Fig. 6. Deposition and escape fraction heatmap of nanoplastics of diameter 1–100 nm under (a) fast breathing condition, (b) middle breathing condition, and (c) slow breathing condition.

range across all lobes. In Fig. 6(b), under middle breathing conditions, the nasal cavity's deposition hotspot shifts to the larynx due to altered airflow dynamics. Deposition in G6 and G7 remains high, influenced by airway geometry, while escape increases, reflecting reduced overall particle-wall interactions. The left lobes, particularly the left inferior lobe, show the most significant percentage of escaped NPs, and the right middle lobes witness a reduction in escape. Fig. 6(c) presents NP behavior under slow breathing. There's a comprehensive reduction in deposition, particularly in the nasal cavity and laryngopharynx for larger NPs (91–100 nm), emphasizing dominance of Brownian diffusion. Despite a general decrease in deposition, the larynx remains a primary deposition site. G6 and G7 continue to exhibit high deposition. Escape increases across all lobes, with the right inferior lung showing the most substantial increase. NPs of 1–10 nm diameter range exhibit the lowest escape among all sizes.

A consistent trend appears: slower breathing conditions facilitate longer transport distances and deeper airway depositions of NPs. Larger NPs generally show reduced transport distances and deeper airway depositions, often registering higher deposition and lower escape than smaller NPs. The larynx consistently serves as a deposition hotspot, while G6 and G7 maintain the highest deposition in the lower airways.

Fig. 7 provides a comprehensive analysis of MPs in the 1–10 μm size range concerning DF and EF under varying respiratory conditions. The DF and EF of MPs ranging from 1 to 100 μm under different breathing conditions are presented in **Supplementary Fig. S1**. In Fig. 7(a), MPs exposed to rapid respiration exhibit distinct deposition sites. Larger MPs (8–10 μm) predominantly deposit in the nasal cavity (52–75.6%), influenced by higher air velocity and turbulence. MPs (5–7 μm) deposit in the laryngopharynx, and 4 μm MPs primarily in the larynx. Smaller MPs (<4 μm) exhibit multi-faceted deposition in upper and lower airways (G6 and G7). Larger MPs (6–10 μm) rapidly deposit in the upper airway, showing limited penetration into deeper regions or escape. Right middle lobe outlets consistently exhibit the lowest EF, decreasing with increasing MP diameter. In Fig. 7(b), under middle breathing conditions, the nasal cavity DF hotspot diminishes, shifting to the laryngopharynx and larynx. There is a general DF reduction for MPs (1–4 μm) and an increase for MPs (>4 μm) compared to rapid breathing. Higher DF in G6 and G7 persists. EF increases overall, notably in the left

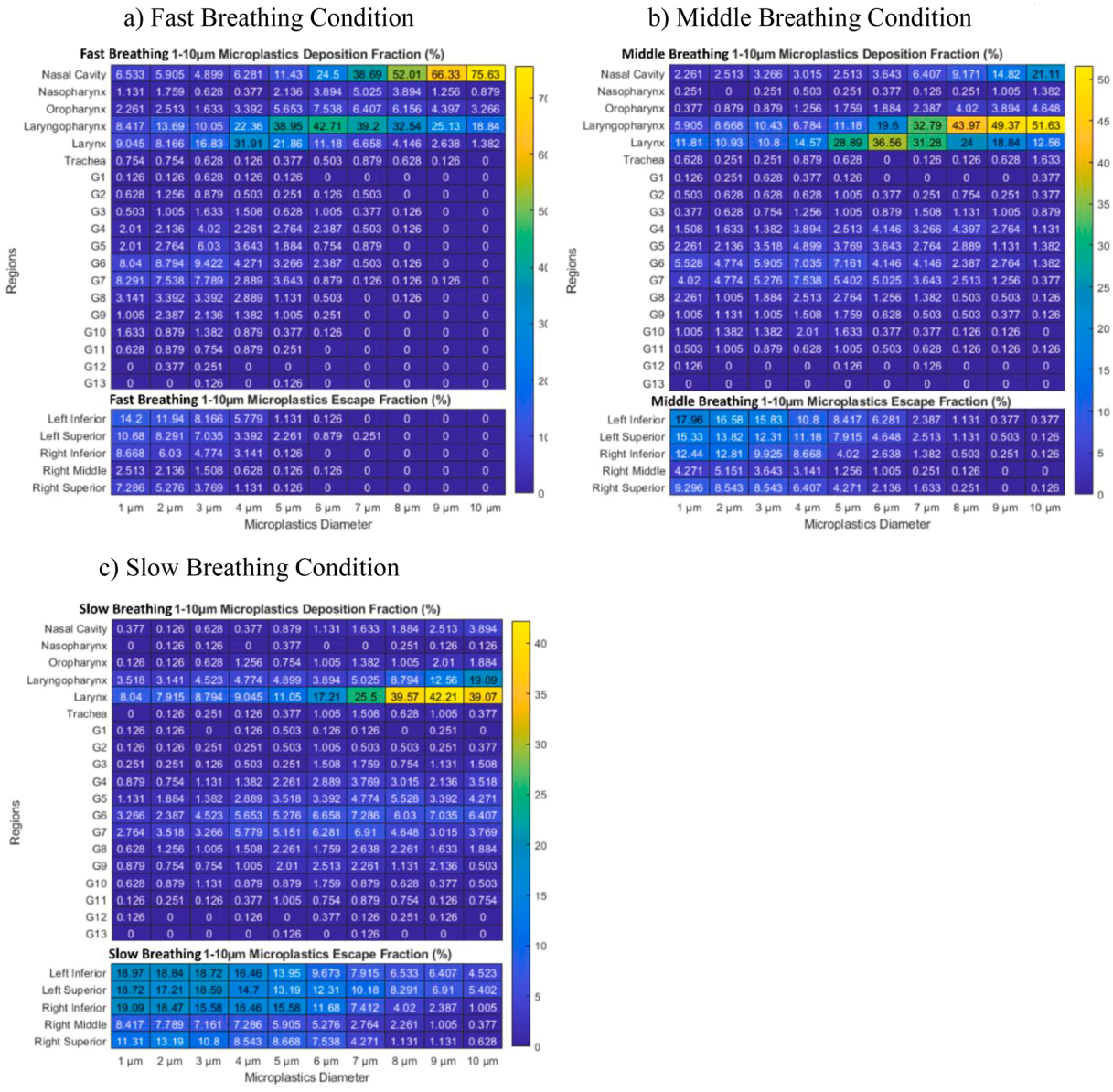

Fig. 7. Deposition and escape fraction heatmap of microplastics of diameter 1–10 μm under (a) fast breathing condition, (b) middle breathing condition, and (c) slow breathing condition.

inferior lobe for 5 μm MPs. The left lobes host the majority of escaped MPs, and the right middle lobes show reduced escape. Fig. 7(c) explores DF and EF under slow breathing. DF decreases throughout, and EF increases, consistent with lower air velocities. The laryngopharynx experiences a significant decline in DF, especially for larger MPs (8–10 μm). The larynx remains the primary deposition site, with G6 and G7 exhibiting high DF. EF increases across all lobes, with the right inferior lung showing the most substantial elevation for 9 μm MPs. Smaller MPs (1 μm) exhibit the highest EF among all MPs, in line with Brownian motion influence.

A consistent pattern can be observed: slower breathing conditions promote greater transport distances and deeper airway depositions of MPs. Notably, 1 μm MPs exhibit the most extended transport distances and deeper airway depositions under all conditions. The DF within the nasal cavity and laryngopharynx declines significantly during the transition from rapid to slow breathing, while DF in the larynx undergoes a more moderate decrease and even an increase for larger MPs. G6 and G7 consistently maintain the highest DF in the lower airways, while G13 records the lowest values. Comparisons between DF and EF patterns for NPs and MPs reveal commonalities. In both cases, the nasal cavity, laryngopharynx, and larynx regions serve as DF hotspots, with G6 and G7 attaining the highest DF in the lower airways. As breathing transitions from rapid to slow, a distinct trend emerges: the higher DF hotspot moves down in anatomical sequence, and EF increases, indicating longer transport distances.

Deposition patterns of non-spherical microplastics

The deposition patterns of cylindrical and tetrahedral non-spherical MPs under normal breathing conditions present notable variations when compared to spherical microplastics and nanoplastics. In the case of cylindrical MPs, as seen in Fig. 8(a) and (c), there is a discernible distribution pattern across the nasal cavity and tracheobronchial tree, with an increased deposition of larger microplastics, especially those ranging from 6 to 15 micrometers in diameter. This distribution can be attributed to the unique aerodynamic behaviors of cylindrical particles under normal breathing conditions, where their orientation and rotation due to airflow dynamics significantly influence their deposition patterns.

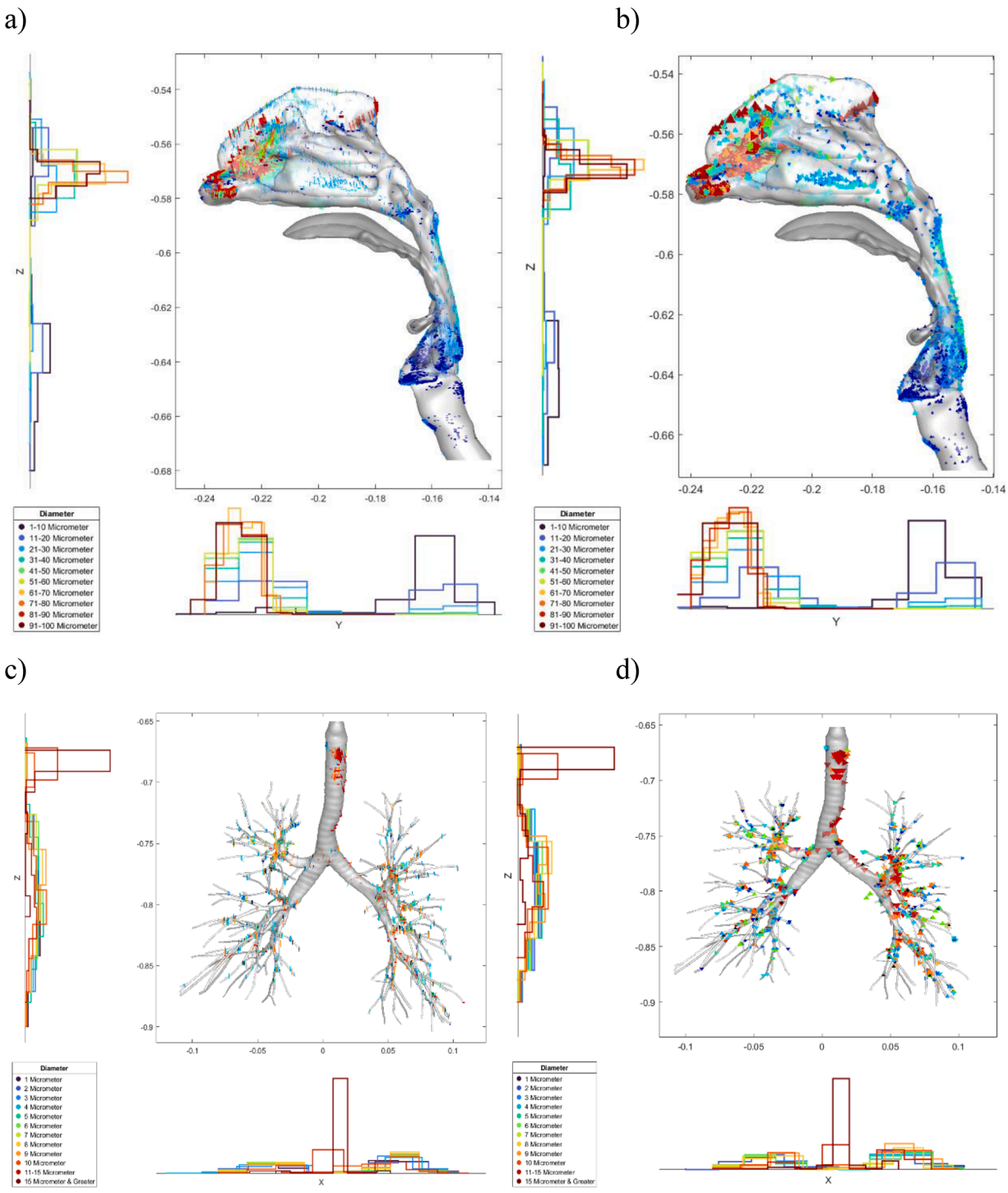

Fig. 8. Deposition and escape fraction heatmap of non-spherical microplastics of diameter 1–100 μm under middle breathing condition: (a) cylindrical particles in the upper airways, (b) tetrahedral particles in the upper airways, (c) cylindrical particles in the lower airways, and (d) tetrahedral particles in the lower airways.

Notably, the deposition is not just confined to the upper airways but extends deeper into the lower respiratory tract, indicating that cylindrical MPs, due to their shape and airflow interactions, can bypass the natural filtration mechanisms more efficiently than their spherical counterparts.

For tetrahedral MPs, Fig. 8(b) and (d) illustrates a different deposition footprint. The sharp edges and corners of these particles contribute a smaller shape factor and provide a distinct aerodynamic profile, which leads to an enhanced deposition in specific areas, particularly in the bifurcation regions of the bronchial tree. The presence of larger tetrahedral MPs in the deeper regions of the lungs suggests that their shape contributes to a more widespread deposition pattern, potentially increasing the risk of deep lung penetration and retention.

Fig. 9 provides a comprehensive analysis of non-spherical MPs in the 1–10 μm size range concerning DF and EF under normal respiratory conditions. For cylindrical MPs, the deposition pattern reveals a higher DF in the nasal cavity compared to tetrahedral MPs, with values peaking for particles between 7 and 9 μm in diameter. This suggests that the elongated shape of cylindrical MPs enhances their retention in the upper respiratory tract. The deposition in the oropharynx and larynx is also

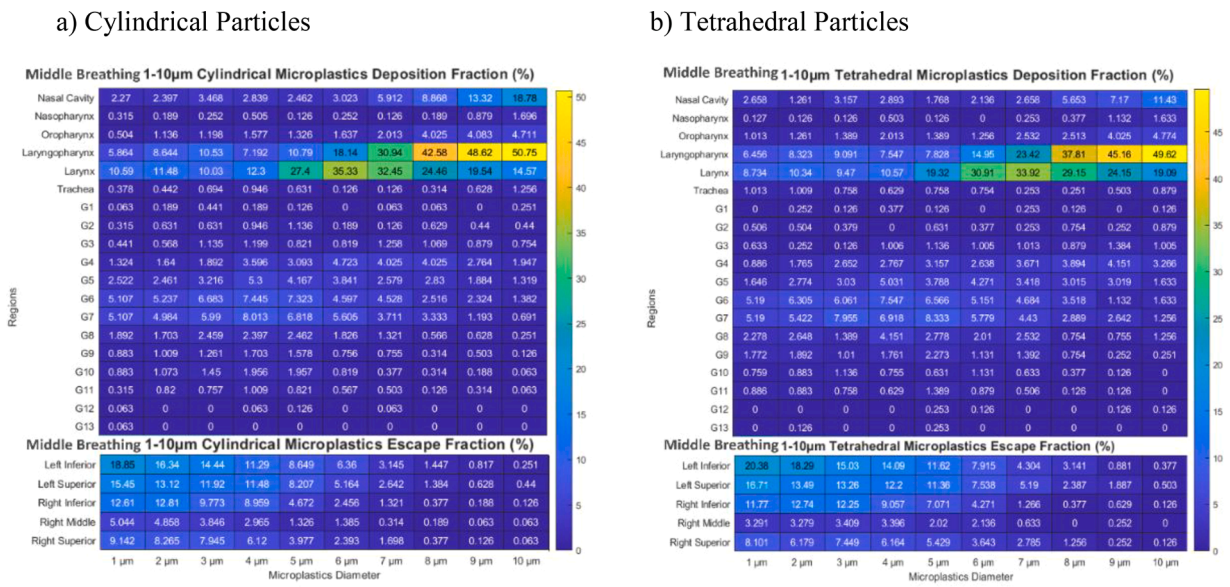

Fig. 9. Deposition and escape fraction heatmap of non-spherical microplastics of diameter 1–10 μm under middle breathing condition: (a) cylindrical particles, and (b) tetrahedral particles.

significant, indicating that these particles are more likely to be deposited in the upper airways compared to spherical particles. Escape fractions for cylindrical MPs exhibit similar tendency and magnitude with that of spherical MPs.

In contrast, tetrahedral MPs show a different deposition pattern. These particles have a higher deposition in the larynx and trachea, which may be due to the irregular shape causing a higher likelihood of impaction in these areas. The nasal cavity sees significant deposition across a broader range of sizes (2–9 μm), suggesting that their shape affects the aerodynamic behavior differently compared to both spherical and cylindrical MPs. Interestingly, tetrahedral MPs exhibit a substantial escape fraction in smaller sizes, particularly in the 1 and 2 μm range, indicating that these sizes can bypass the upper respiratory defenses more effectively.

Overall, tetrahedral MPs, with smaller shape factor, may travel deeper into the respiratory tract, whereas cylindrical MPs, with their irregular shape, might experience more turbulence and thus have a different deposition pattern. These findings highlight the importance of considering particle shape, in addition to size and respiration rate, when assessing the respiratory deposition and potential health impacts of inhaled MPs. The distinct deposition and escape patterns of cylindrical and tetrahedral MPs suggest that they may pose different health risks compared to spherical MPs. Therefore, risk assessments for inhaled MPs should take into account the shape of the particles, as it significantly influences their deposition within the respiratory system.

Potential health risk

Recent investigations have highlighted the significant impact of nano- and microplastics on respiratory health, adding a new dimension to the environmental and health risks associated with these particles. In line with our findings, research has demonstrated that even low concentrations of microplastics, such as polystyrene, can significantly alter lung surfactant compositions, leading to increased formation of hydroxyl radicals and potential respiratory health risks (Shi et al., 2022). This is particularly concerning given the essential role of lung surfactants in maintaining lung stability and preventing alveolar collapse. Our study's results are consistent with these findings, showing that a large percentage of NMPs can transport and deposit in the dismal lung, indicating risk for surfactant damage at deep generations of lung.

Furthermore, studies on tire wear microplastic particles have provided evidence of pulmonary toxic effects, including restricted ventilatory function and fibrotic changes in lung tissues (Li et al., 2022). These insights complement our findings by providing an experimental result of how NMPs smaller than 1 μm can contribute to lung injury and fibrosis.

Conclusion

This study presents a groundbreaking and comprehensive investigation into the dynamics of nano- and microplastic transport and deposition throughout the human respiratory tract under diverse breathing conditions. Key insights derived from our research are as follows:

1. Distinct Deposition Patterns: Noteworthy differences in deposition patterns were observed for MPs and NPs across varying breathing rates. Slower breathing rates were found to significantly enhance the deposition coverage of MPs, particularly within critical regions such as the nasal cavity, laryngopharynx, and larynx.
2. Breathing Rate Influence: The breathing rate is a crucial factor influencing the deposition and escape dynamics of NMPs. Faster breathing rates led to heightened deposition in the upper respiratory tract, particularly for larger MPs, whereas slower breathing facilitated deeper penetration and deposition of smaller NPs.
3. Identification of Deposition Hotspots: Specific hotspots within the respiratory tract were identified where NMPs preferentially deposit. Larger MPs exhibited a concentration in the anterior segment of the nasal cavity, while both smaller NPs and MPs demonstrated a more even distribution throughout the airway.
4. Critical Role of Particle Size: The size of NMPs emerged as a critical determinant in governing their transport and deposition patterns. Larger MPs displayed a tendency for rapid deposition in the upper airways, whereas smaller NPs exhibited a higher likelihood of escape or reaching deeper airway generations.
5. Non-spherical MPs have a propensity for deeper lung penetration compared to spherical microplastics and nanoplastics, potentially leading to different health outcomes.

These findings highlight the imperative consideration of breathing rates and particle sizes in health risk assessments associated with respiratory exposure to NMPs. Such insights are essential for the

development of targeted strategies aimed at mitigating potential health risks and ensuring effective health interventions.

Limitations of methodology

The current study acknowledges certain simplifications in the modeling of micro and nanoparticles transport within the respiratory tract. Notably, intricate phenomena such as the evaporation of the mucus layer and the hygroscopic nature of particles are not considered in the present analysis. Additionally, the respiratory motion involving the contraction and expansion of the airway wall is not explicitly modeled in this study. These simplifications, while facilitating a foundational understanding, should be recognized as limitations that may impact the comprehensive representation of real-world respiratory dynamics.

Future studies

To enhance our comprehension of NMPs' behavior within the human respiratory tract, future investigations should strive to construct an advanced computational model that extends its coverage to include the alveolar sacs. Additionally, incorporating the dynamic motion of the airway walls into the model would represent a significant improvement. Moreover, the mucociliary clearance, as well as the NMP's surface charges' interactions with the electromagnetic fields in the context of human biology should be investigated in the future. These advancements would offer a more comprehensive exploration of particle deposition, providing heightened precision in predictions.

CRediT authorship contribution statement

Xinlei Huang: Formal analysis, Software, Writing – original draft. **Suvash C. Saha:** Conceptualization, Supervision, Writing – review & editing. **Goutam Saha:** Validation, Writing – review & editing. **Isabella Francis:** Software, Writing – review & editing. **Zhen Luo:** Supervision, Writing – review & editing.

Declaration of competing interest

The authors declare no potential conflicts of interest with respect to the research, authorship, and publication of this article.

Data availability

Data will be made available on request.

Acknowledgments

The authors would like to acknowledge the computing facility at the University of Technology Sydney (UTS). The authors used AI-assisted technology (ChatGPT 4) for language editing and grammar checking.

Supplementary materials

Supplementary material associated with this article can be found, in the online version, at doi:10.1016/j.envadv.2024.100525.

References

Ahookhosh, K., Yaqoubi, S., Mohammadpourfard, M., Hamishehkar, H., Aminfar, H., 2019. Experimental investigation of aerosol deposition through a realistic respiratory airway replica: An evaluation for MDI and DPI performance. Int. J. Pharm. 566, 157.

ANSYS, 2020. ANSYS Fluent Theory Guide. ANSYS, Inc., 2600 ANSYS Drive Canonsburg, PA 15317

Baeza-Martinez, C., Olmos, S., Gonzalez-Pleiter, M., Lopez-Castellanos, J., Garcia-Pachon, E., Masia-Canuto, M., Hernandez-Blasco, L., Bayo, J., 2022. First evidence of microplastics isolated in European citizens' lower airway. J. Hazard. Mater. 438, 129439.

Browne, M.A., Crump, P., Niven, S.J., Teuten, E., Tonkin, A., Galloway, T., Thompson, R., 2011. Accumulation of Microplastic on Shorelines Woldwide: Sources and Sinks. Environ. Sci. Technol. 45, 9175.

Chen, Q., Gao, J., Yu, H., Su, H., Yang, Y., Cao, Y., Zhang, Q., Ren, Y., Hollert, H., Shi, H., Chen, C., Liu, H., 2022. An emerging role of microplastics in the etiology of lung ground glass nodules. Environ. Sci. Eur. 34.

Cohen, B., Sussman, R., Lippmann, M., 1990. Ultrafine particle deposition in a human tracheobronchial cast. Aerosol. Sci. Technol. Aerosol. Sci. Tech. 12, 1082.

Dichgans, F., Boos, J.-P., Ahmadi, P., Frei, S., Fleckenstein, J.H., 2023. Integrated numerical modeling to quantify transport and fate of microplastics in the hyporheic zone. Water. Res. 243, 120349.

Dong, C.D., Chen, C.W., Chen, Y.C., Chen, H.H., Lee, J.S., Lin, C.H., 2020. Polystyrene microplastic particles: *in vitro* pulmonary toxicity assessment. J. Hazard. Mater. 385, 121575.

Dries, D.J., Endorf, F.W., 2013. Inhalation injury: epidemiology, pathology, treatment strategies. Scand. J. Trauma Resusc. Emerg. Med. 21, 31.

Du, F., Cai, H., Zhang, Q., Chen, Q., Shi, H., 2020. Microplastics in take-out food containers. J. Hazard. Mater. 399, 122969.

Elagami, H., Frei, S., Boos, J.-P., Trommer, G., Gilfedder, B.S., 2023. Quantifying microplastic residence times in lakes using mesocosm experiments and transport modelling. Water. Res. 229, 119463.

Fatahi, M., Akdogan, G., Dorfling, C., Wyk, P.V., 2021. Numerical study of microplastic dispersal in simulated coastal waters using CFD approach. Water 13, 3432 (Basel).

Feng, Y., Tu, C., Li, R., Wu, D., Yang, J., Xia, Y., Peijnenburg, W.J.G.M., Luo, Y., 2023. A systematic review of the impacts of exposure to micro- and nano-plastics on human tissue accumulation and health. Eco Environ. Health 2, 195.

Hashizume, M., Kim, Y., Ng, C.F.S., Chung, Y., Madaniyazi, L., Bell, M.L., Guo, Y.L., Kan, H., Honda, Y., Yi, S.-M., Kim, H., Nishiwaki, Y., 2020. Health effects of Asian dust: a systematic review and meta-analysis. Environ. Health Perspect. 128, 066001.

Horsfield, K., Dart, G., Olson, D.E., Filley, G.F., Cumming, G., 1971. Models of the human bronchial tree. J. Appl. Physiol. 31, 207.

Islam, M.S., Saha, S.C., Sauret, E., Gemci, T., Gu, Y.T., 2017. Pulmonary aerosol transport and deposition analysis in upper 17 generations of the human respiratory tract. J. Aerosol. Sci. 108, 29.

Islam, S., Rahman, M., Larpruenrudee, P., Arsalanloo, A., Mortazavy Beni, H.R., Gu, Y., Sauret, E., 2023. How microplastics are transported and deposited in realistic upper airways? Phys. Fluids 35.

Jenner, L.C., Rotchell, J.M., Bennett, R.T., Cowen, M., Tentzeris, V., Sadofsky, L.R., 2022. Detection of microplastics in human lung tissue using muFTIR spectroscopy. Sci. Total. Environ. 831, 154907.

Jiang, Y., Han, J., Na, J., Fang, J., Qi, C., Lu, J., Liu, X., Zhou, C., Feng, J., Zhu, W., Liu, L., Jiang, H., Hua, Z., Pan, G., Yan, L., Sun, W., Yang, Z., 2022. Exposure to microplastics in the upper respiratory tract of indoor and outdoor workers. Chemosphere 307, 136067.

Khajeh-Hosseini-Dalasm, N., Longest, P.W., 2015. Deposition of particles in the alveolar airways: inhalation and breath-hold with pharmaceutical aerosols. J. Aerosol. Sci. 79, 15.

Kolanjiyil, A.V., Kleinstreuer, C., 2017. Computational analysis of aerosol-dynamics in a human whole-lung airway model. J. Aerosol. Sci. 114, 301.

Koullapis, P.G., Stylianou, F.S., Sznitman, J., Olsson, B., Kassinos, S.C., 2020. Towards whole-lung simulations of aerosol deposition: a model of the deep lung. J. Aerosol. Sci. 144.

B. Kumar, V. Srivastav, A. Jain, and A. Paul, "Study of numerical schemes for the CFD simulation of human airways," 32 (2019).

Lehner, R., Weder, C., Petri-Fink, A., Rothen-Rutishauser, B., 2019. Emergence of nanoplastic in the environment and possible impact on human health. Environ. Sci. Technol. 53, 1748.

Li, Y., Shi, T., Li, X., Sun, H., Xia, X., Ji, X., Zhang, J., Liu, M., Lin, Y., Zhang, R., Zheng, Y., Tang, J., 2022. Inhaled tire-wear microplastic particles induced pulmonary fibrotic injury via epithelial cytoskeleton rearrangement. Environ. Int. 164, 107257.

Liu, H., Zhou, X., Ding, W., Zhang, Z., Nghiem, L.D., Sun, J., Wang, Q., 2019. Do microplastics affect biological wastewater treatment performance? implications from bacterial activity experiments. ACS. Sustain. Chem. Eng. 7, 20097.

Longest, P.W., Bass, K., Dutta, R., Rani, V., Thomas, M.L., El-Achwah, A., Hindle, M., 2019. Use of computational fluid dynamics deposition modeling in respiratory drug delivery. Expert. Opin. Drug Deliv. 16, 7.

Lu, W., Li, X., Wang, S., Tu, C., Qiu, L., Zhang, H., Zhong, C., Li, S., Liu, Y., Liu, J., Zhou, Y., 2023. New evidence of microplastics in the lower respiratory tract: inhalation through smoking. Environ. Sci. Technol. 57, 8496.

Ma, B., Lutchen, K.R., 2009. CFD simulation of aerosol deposition in an anatomically based human large-medium airway model. Ann. Biomed. Eng. 37, 271.

Napper, E., Bakir, A., Rowland, S.J., Thompson, R.C., 2015. Characterisation, quantity and sorptive properties of microplastics extracted from cosmetics. Mar. Pollut. Bull. 99, 178.

Nishi, M., 2004. Breathing of Humans and Its Simulation. LSTM-Erlangen Institute of Fluid Mechanic Friedlich-Alexander-University Erlangen.

Osseiran, N., 2019. WHO Calls for More Research into Microplastics and A Crackdown on Plastic Pollution. World Health Organization, Geneva.

Prata, J.C., da Costa, J.P., Lopes, I., Duarte, A.C., Rocha-Santos, T., 2020. Environmental exposure to microplastics: an overview on possible human health effects. Sci. Total Environ. 702, 134455.

Quyen, L.D., Choi, J.M., 2022. Accumulation and dispersion of microplastics near a submerged structure: basic study using a numerical wave tank. J. Mar. Sci. Eng. 10, 1934.
Quyen, L.D., Park, Y.-G., Lee, I.-c., Choi, J.M., 2024. CFD analysis of microplastic transport over the slopes. J. Mar. Sci. Eng. 12, 145.
Saha, S.C., Saha, G., 2024. Effect of microplastics deposition on human lung airways: a review with computational benefits and challenges. Heliyon 10, e24355.
Saha, S., Francis, I., Huang, X., Paul, A., 2022. Heat transfer and fluid flow analysis of realistic 16-generation lung. Phys. Fluids 34.
Sakai, Y., Manhart, M., 2024. Direct numerical simulation of the distribution of floating microplastic particles in an open channel flow. Appl. Res. 3, e202200092.
Shamskhany, A., Karimpour, S., 2022. Entrainment and vertical mixing of aquatic microplastics in turbulent flow: The coupled role of particle size and density. Mar. Pollut. Bull. 184, 114160.
Shi, W., Cao, Y., Chai, X., Zhao, Q., Geng, Y., Liu, D., Tian, S., 2022. Potential health risks of the interaction of microplastics and lung surfactant. J. Hazard. Mater. 429, 128109.
Stapleton, P.A., 2019. Toxicological considerations of nano-sized plastics. AIMS. Environ. Sci. 6, 367.
Tokunaga, Y., Okochi, H., Tani, Y., Niida, Y., Tachibana, T., Saigawa, K., Katayama, K., Moriguchi, S., Kato, T., Hayama, S.I., 2023. Airborne microplastics detected in the lungs of wild birds in Japan. Chemosphere 321, 138032.
Wedel, J., Steinmann, P., Štrakl, M., Hriberšek, M., Cui, Y., Ravnik, J., 2022. Anatomy matters: The role of the subject-specific respiratory tract on aerosol deposition - A CFD study. Comput. Methods Appl. Mech. Eng. 401, 115372.
Worth Longest, P., Vinchurkar, S., 2007. Validating CFD predictions of respiratory aerosol deposition: effects of upstream transition and turbulence. J. Biomech. 40, 305.
Xi, J., Longest, P.W., 2009. Characterization of submicrometer aerosol deposition in extrathoracic airways during nasal exhalation. Aerosol. Sci. Technol. 43, 808.
Yang, H., Foroutan, H., 2023. Effects of near-bed turbulence on microplastics fate and transport in streams. Sci. Total Environ. 905, 167173.
Yang, T., Wang, J., 2023. Exposure sources and pathways of micro- and nanoplastics in the environment, with emphasis on potential effects in humans: a systematic review. Integr. Environ. Assess. Manag.
Yee, M.S., Hii, L.W., Looi, C.K., Lim, W.M., Wong, S.F., Kok, Y.Y., Tan, B.K., Wong, C.Y., Leong, C.O., 2021. Impact of microplastics and nanoplastics on human health. Nanomaterials 11 (Basel).
Zhang, Z., Liu, H., Wen, H., Gao, L., Gong, Y., Guo, W., Wang, Z., Li, X., Wang, Q., 2021. Microplastics deteriorate the removal efficiency of antibiotic resistance genes during aerobic sludge digestion. Sci. Total Environ. 798, 149344.
Zhang, J., Ji, C., Liu, G., Zhang, Q., Xing, E., 2023. Settling processes of cylindrical microplastics in quiescent water: a fully resolved numerical simulation study. Mar. Pollut. Bull. 194, 115438.
Zuo, Y.Y., Veldhuizen, R.A., Neumann, A.W., Petersen, N.O., Possmayer, F., 2008. Current perspectives in pulmonary surfactant–inhibition, enhancement and evaluation. Biochim. Biophys. Acta 1778, 1947.